

# A Generic Trajectory Planning Method for Constrained All-Wheel-Steering Robots

Ren Xin<sup>1,2</sup>, Hongji Liu<sup>1,2</sup>, Yingbing Chen<sup>1,2</sup>, Sheng Wang<sup>1,2</sup> and Ming Liu<sup>1,3</sup>

**Abstract**—This paper presents a trajectory planning method for wheeled robots with fixed steering axes while the steering angle of each wheel is constrained. In the past, All-Wheel-Steering (AWS) robots, incorporating modes such as rotation-free translation maneuvers, in-situ rotational maneuvers, and proportional steering, exhibited inefficient performance due to time-consuming mode switches. This inefficiency arises from wheel rotation constraints and inter-wheel cooperation requirements. The direct application of a holonomic moving strategy can lead to significant slip angles or even structural failure. Additionally, the limited steering range of AWS wheeled robots exacerbates nonlinearity issues, thereby complicating control processes. To address these challenges, we developed a novel planning method termed Constrained AWS (C-AWS), which integrates second-order discrete search with predictive control techniques. Experimental results demonstrate that our method adeptly generates feasible and smooth trajectories for C-AWS while adhering to steering angle constraints. Code and video can be found at <https://github.com/Rex-sys-hk/AWSPlanning>.

## I. INTRODUCTION

### A. Motivation

The benefits of the omnidirectional wheel chassis, particularly during low-speed maneuvers, are well-recognized, enabling operations like spot turning and translation that are unfeasible with traditional platforms with Ackerman geometry [1], [2]. However, the intricacy and lack of intuitiveness in the human-machine interaction for All-Wheel-Steering (AWS) vehicles have hampered their widespread usage [3].

The advent of autonomous driving technologies is improving the functionality of all-wheel-steering robots, making their control more manageable. Autonomous operation requires consideration of the rotation angles and speeds of all wheels, introducing complexities absent in the simplified motion control of Ackerman geometry [4]. The concept of the Instantaneous Center of Motion (ICM) [5], is widely employed in describing the motion of rigid bodies, to make sure coherence in the motion states of each wheel. ICM theory posits that the motion of a rigid body can be simplified as rotational motion around a specific center, characterized by angular velocity and radius. However, the ICM model exhibits two singular conditions when rotating radius approaching 0 or infinity, potentially leading to scenarios where the controller lacks a viable solution or may even

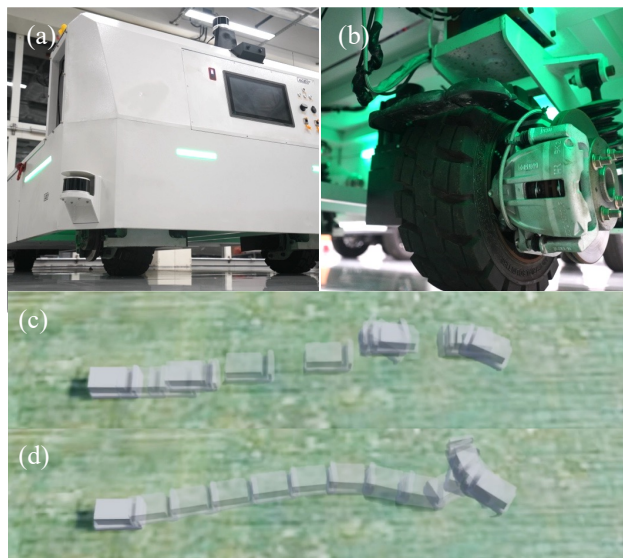


Fig. 1. (a) Depicts a typical autonomous airport baggage carrier, equipped with LiDAR, cameras, computing units and AWS chassis. (b) Illustrates the design of the vehicle’s steering wheel. The image reveals that despite the wheel’s ability to rotate via the top-mounted steering motor, its free rotation is constrained by essential circuits and hydraulic systems. (c) and (d) demonstrate the operation of the AWS vehicle through mode switching and the movement optimization achieved by the proposed C-AWS algorithm, respectively.

crash. Christian *et al.* [6] remapped the rotation radius to a periodic function using spherical coordinates to address the **singularity** problem of the ICM method when the rotating radius approaches infinity. Nevertheless, Christian *et al.* only solves the mapping relationship between moving speed, wheel walking speed, and steering angle, but cannot solve the robot motion control problem. This method does not ensure that the vehicle can effectively follow a path. Reza *et al.* [7], [8] comprehensively defined the path-following problem for AWS robots, considering wheel velocity constraints. They estimated the maximum speed for each wheel to achieve time optimality and considered the remaining trajectory length to prioritize either distance minimization or angle error reduction. However, their model does not address **acceleration constraints**, leading to frequent wheel oscillations and significant acceleration when tracking specific directional trajectories. In addition, AWS platforms have problems with **steering constraints**. For example, airport baggage carriers confined to a steering range of  $\pm 90^\circ$  [9], attributed to factors like structural durability, hydraulic and electric system requirements, as illustrated in fig. 1(a),(b). Traditionally, to circumvent constraints, practitioners treated motion within a specific constraint range as a distinct driving

<sup>1</sup>The Hong Kong University of Science and Technology (Guangzhou), Nansha, Guangzhou, 511400, Guangdong, China. <sup>2</sup>The Hong Kong University of Science and Technology, Hong Kong SAR, China. <sup>3</sup>HKUST Shenzhen-Hong Kong Collaborative Innovation Research Institute, Futian, Shenzhen, China. (Email: {rxin, hliucq, ychengz, swangei}@connect.ust.hk, eelium@hkust-gz.edu.cn).

mode and manually switched between these modes, leading to a reduction in movement flexibility for the AWS chassis as demonstrated in fig. 1(c).

### B. Contribution

To enhance the operating efficiency of Constrained AWS(C-AWS) platforms, smoothness, and reliability under constrained conditions, we adopt a predictive control strategy. Our approach involves initially identifying a viable trajectory to the target pose and subsequently refining it to minimize travel time within given constraints. The trajectory search accounts for both the feasibility and cost related to wheel movement, as well as the connectivity within the configuration space. Consequently, we introduced the time-cost-2nd-order hybrid A\* [10] method for initial trajectory searching, which evaluates wheel conditions and integrates traveling cost into time consumption. In this way, the planner can search for efficient driving mode priors instead of manually defining them. In the optimization process, our method referred to the Model Predictive Control (MPC) framework, emphasizing the need for a motion state equation that is third-order differentiable and continuous to adhere to **acceleration constraints**. Given that the control model by Christian *et al.* [6] exhibits **singularity** in steering angle and lacks differentiability when rotation radius is 0, we integrated a differentiable rigid body motion description [11] with **steering constraints**. This integration was facilitated by introducing intermediary variables to circumvent the robot state singularities problem and linearizing the constraint expressions.

Our contributions are three-fold:

- 1) The time-cost-2nd-order initial trajectory planner, which is widely suitable for robots with fixed steering axis positions.
- 2) The universal smoother that incorporates our kinematic model, linearizing steering constraints to generate feasible paths and control mechanisms for C-AWS.
- 3) Digital twinning of the experimental platform and the conduction of experiments in a simulation environment verifying the effectiveness of our method.

## II. RELATED WORKS

### A. Kinematic Models

Kinematic models are represented as ordinary differential equations. These equations describe the relationship between the changing states and their rates of change over time. Mass point models are a simplified representation where moving states are linearly additive, like when the heading of the controlled object is independent of its motion. This model is suitable for holonomic moving platforms equipped with Macnumm wheels [12]. Control problems of such models can be classified as Linear Programming (LP) problems and can usually be solved with simple negative feedback control or Linear Quadratic Regulator (LQR). Nonlinear dynamic models are used to describe physical systems with dependent states. Controlling with this kind of model typically involves numerical Nonlinear Programming (NLP) solving methods. For instance, single-wheel models are used on differential

steering wheeled robots [13], which adjust the speed difference between drive wheels to change the facing direction of the vehicle and adjust its moving direction. The bicycle model is another nonlinear model simplifying the mathematical representation of the dynamics of vehicles with Ackerman geometry. This model captures the essential motion features of vehicles like bicycles, whose rear wheels cannot be steered or whose rear wheels are steered in a certain proportion [14], and even trailers [15]. The steering angle has an injective relationship to the curvature of an arc tangent to the heading direction at a specific point. In contrast to the aforementioned nonlinear dynamic models, AWS robots allow for dynamic adjustment of the rotating center. This transforms the control of lateral movement from one-dimensional to two-dimensional, significantly enhancing the robot's mobility. However, in the planning and control of AWS robots, the relationship between the wheel's steering angle and the motion state is non-injective and is further complicated by substantial inter-wheel constraints. These issues amplify the non-linearity and discontinuity of the model, rendering it unsuitable for direct resolution through NLP solvers. In our C-AWS algorithm, we reformulated this problem to enable its solution using Nonlinear Programming (NLP) solvers.

### B. Trajectory Planning

Trajectory planning is a process that generates a feasible and followable path for a robot, assigning specific speed and pose requirements at certain time steps. This process is governed by two core criteria: ensuring the trajectory is collision-free and trackable [16]. Sampling-based methods are popular in robotics for finding collision-free paths due to their versatility in incorporating user-defined objectives. These methods encompass state lattice [17], [18] approaches and probabilistic planners. They essentially operate by sampling the robot's possible states within the configuration space to discover a viable trajectory between the start and goal nodes. Lattice-based planners break down the continuous state space into a discrete lattice graph structure for planning purposes. Subsequently, algorithms such as Dijkstra's algorithm are applied to identify the optimal trajectory through this graph. Excluding lattice planners, probabilistic planners exemplified by Rapidly-exploring Random Trees (RRT) [19] generate a feasible path by iteratively growing a tree of states starting from the initial node. The sampling process inherent in these methods [10], [20], [21] accounts for the vehicle's dynamic constraints. In the process of searching for paths, piecewise parametric curves are extensively used. For example, Dubins' paths [22] and Reed-Shepp's paths [23] decompose complex paths into sequences of simpler maneuvers, such as constant turning and straight-line motion. Meanwhile, spiral curves facilitate gradual changes in direction and speed [24]. Specifically, the forward movement of bicycles can be modeled as an arc, ensuring feasibility for non-holonomic models. Therefore, our time-cost-2nd-order trajectory searching method has been developed based on the hybrid A\* algorithm which can efficiently take advantage of this feature.

MPC techniques address trajectory planning by conceptualizing it as an Optimal Control Problem (OCP), subsequently transformed into a Nonlinear Programming (NLP) problem [25]–[27]. Regarding the functionality of MPC, our algorithm employs this framework with meticulous model design and high-quality initial guesses. Trajectory optimization for vehicles at each timestep utilizes differentiable curves or numerical methods to maintain state continuity. Differentiable curves like splines are generated by interpolating between control points [28] while polynomials are determined by coefficients [29]. However, the use of parameterized curves introduces bias related to curve property or degree of freedom. To solve these trajectory optimization problems numerically, methods such as Euler [30] and advanced Runge-Kutta (RK) algorithms are employed in our method. Specifically, we utilize the RK4 algorithm, which strikes a balance between accuracy and computational efficiency.

### III. METHODOLOGY

#### A. Rigid Body Vehicle Model

First, we define the state variables and control variables of the system as an arbitrary rigid body

$$\mathbf{x} = [x, y, \theta, \dot{x}, \dot{y}, \dot{\theta}]^\top,$$

$$\mathbf{u} = [\ddot{x}, \ddot{y}, \ddot{\theta}]^\top,$$

where  $x, y, \theta$  are the essential descriptions of 2D movement of a rigid body: position and heading angle. The wheel positions regarding the robot frame are defined as

$$\mathbf{W} := \{\mathbf{w}_i | \mathbf{w}_i \in \mathbb{R}^2, i \in \{1, 2, \dots, N_w\}\},$$

and steering limits for each wheel are defined as

$$\bar{\mathcal{D}}_{lim} := \{\bar{\delta}_{lim, w_i} | \bar{\delta}_{lim, w_i} \in \mathbb{R}, \text{ for } w_i \in \mathbf{W}\},$$

$$\underline{\mathcal{D}}_{lim} := \{\underline{\delta}_{lim, w_i} | \underline{\delta}_{lim, w_i} \in \mathbb{R}, \text{ for } w_i \in \mathbf{W}\}.$$

The location of a rigid body in 2D space can be represented by SE(2)

$$\begin{bmatrix} \mathbf{R} & \mathbf{p} \\ 0 & 1 \end{bmatrix} \text{ where } \mathbf{R} \in SO(2) \text{ and } \mathbf{p} \in \mathbb{R}^2,$$

where the rotation matrix and position vector are

$$\mathbf{R}(\theta) = \begin{bmatrix} \cos \theta & -\sin \theta \\ \sin \theta & \cos \theta \end{bmatrix}, \mathbf{p} = \begin{bmatrix} x \\ y \end{bmatrix}.$$

By deriving the rotation and position transformation regarding  $t$  respectively, we can get

$$\omega(\theta) = \frac{\partial \mathbf{R}(\theta)}{\partial t} = \frac{\partial}{\partial t} \begin{bmatrix} \cos \theta & -\sin \theta \\ \sin \theta & \cos \theta \end{bmatrix}$$

$$= \begin{bmatrix} -\sin \theta & -\cos \theta \\ \cos \theta & -\sin \theta \end{bmatrix} \cdot \dot{\theta}$$

$$= \mathcal{K}(\theta) \dot{\theta},$$

$$\mathbf{v} = \frac{\partial \mathbf{p}}{\partial t} = \begin{bmatrix} \dot{x} \\ \dot{y} \end{bmatrix}.$$

Since the instantaneous motion of the vehicle can be regarded as a rotation around a certain point, in order to calculate the motion of each point on the vehicle body,

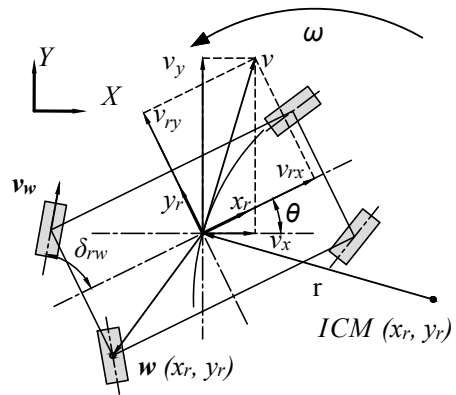


Fig. 2. The schematic representation of an AWS robot kinematic model. Please note the  $\omega$  direction only indicates the positive direction, not the rotating direction at the instance.

we obtain the position of the instantaneous center which is indicated by the radius vector

$$\mathbf{r}_{ICM} = \omega^{-1}(\theta) \mathbf{v} = \mathcal{K}(\theta)^\top \begin{bmatrix} \dot{x} \\ \dot{y} \\ \dot{\theta} \end{bmatrix}, \quad (1)$$

where  $\mathbf{r}_{ICM}$  stands for the vector point from the relative center of the ICM position pointing to the vehicle control center **in the robot frame**. Here we introduced the wheel moving velocity as an intermediate variable. For each wheel ground contacting position, the required moving velocity in the world frame can be computed by

$$\mathbf{r}_{ICM, w} = \mathbf{r}_{ICM} + \mathbf{w},$$

$$\mathbf{v}_w = \omega(\theta) \cdot \mathbf{r}_{ICM, w} = \mathbf{v} + \omega(\theta) \mathbf{w},$$

while the wheel moving speed regarding robot heading is

$$\mathbf{v}_{r, w} = \mathbf{R}(\theta)^{-1} \mathbf{v}_w = \mathbf{R}(\theta)^\top \mathbf{v}_w, \quad (2)$$

the steering angle can be written as

$$\delta_w = \arctan_2(v_{wy}, v_{wx}) = 2 \arctan \left( \frac{v_{wy}}{|\mathbf{v}_w| + v_{wx}} \right), \quad (3)$$

and in the robot frame, it would be

$$\delta_{r, w} = \delta_w - \theta. \quad (4)$$

The time derivative of  $\mathbf{v}_w$  is

$$\frac{\partial \mathbf{v}_w}{\partial t} = \frac{\partial \mathbf{v}}{\partial t} + \frac{\partial \omega(\theta)}{\partial t} \mathbf{w}$$

$$= \begin{bmatrix} \ddot{x} \\ \ddot{y} \end{bmatrix} + \begin{bmatrix} -\cos \theta & \sin \theta \\ -\sin \theta & -\cos \theta \end{bmatrix} \dot{\theta}^2 \mathbf{w}$$

$$+ \begin{bmatrix} -\sin(\theta) & -\cos(\theta) \\ \cos(\theta) & -\sin(\theta) \end{bmatrix} \ddot{\theta} \mathbf{w}. \quad (5)$$

and time derivative of  $\delta_w$  is,

$$\frac{\partial \delta_w}{\partial t} = \frac{\partial \arctan_2(v_{wy}, v_{wx})}{\partial t}$$

$$= \frac{-v_{wy} \dot{v}_{wx} v_w + v_{wx} \dot{v}_{wy} v_w - v_{wx} v_{wy} - v_w^2 v_{wy} + v_w^2 \dot{v}_{wy}}{2v_w^2 (v_w + v_{wx})}. \quad (6)$$

Nevertheless, it is not used in the optimizing process together with eq. 3, eq. 4 to avoid discontinuity and singularity.

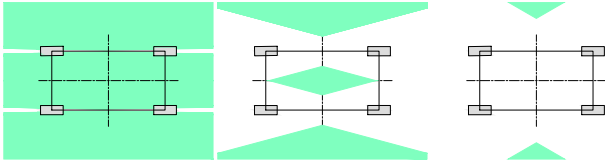


Fig. 3. Feasible ICM regions near control center are marked green, here we show feasible regions when  $\delta_{lim} = 90^\circ, 75^\circ, 60^\circ$ .

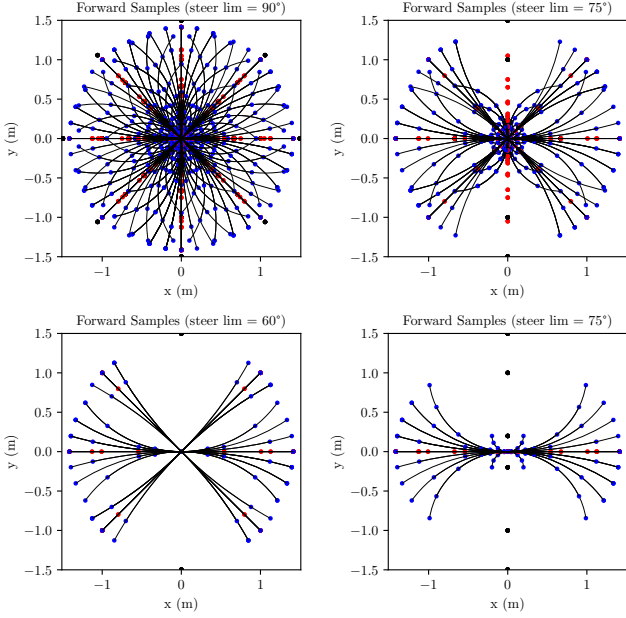


Fig. 4. The sampled maneuvers with  $\delta_{lim} = 90^\circ, 75^\circ, 60^\circ$  and front-75°-rear-0° respectively. The red points are the end of the velocity vector, the blue points are the end of trajectories, and the black points are instantaneous centers. In all the forward samples above,  $N$  of  $\mathcal{E}$  is 8,  $N$  of  $\Psi$  is 8, and  $\omega$  are uniformly sampled 8 times in range  $[-\pi/2, \pi/2]$ .

### B. Path Initialization

To offer a high-quality feasible route for the optimizer, a global planning method based on HybridA\* is developed. In our design, not only the first-order states like position and heading are sampled, but also the body velocity is sampled and recorded. We simplify the integration process from high-order variables to low-order variables, which is a tradeoff in calculation time and accuracy. For the forward simulation process, we customized the grid sampling method for this all-wheel steering chassis. To encourage that each sampling explores new states, we conduct grid sampling of ICM on the spherical coordinate. The feasible ICM location regarding steering limits is shown in Fig. 3. It must be within the intersection of the areas that the normals of the movement directions of all wheels can pass through.

The radius vector  $\mathbf{r}$  points from ICM to the vehicle control center is used here again to represent the moving states. Two variables  $\varepsilon$  and  $\psi$  are uniformly sampled variables on the coordinate axes of the spherical coordinate system, which can

be written as

$$\mathcal{E} : \left\{ \varepsilon_i \mid \varepsilon_i = \frac{\pi i + \varepsilon}{2N + \varepsilon}, \forall i \in \{0, 1, \dots, N\} \right\},$$

$$\Psi : \left\{ \psi_i \mid \psi_i = -\pi + \frac{2\pi i}{N}, \forall i \in \{0, 1, \dots, N\} \right\}.$$

On the grid mesh points constructed by the two sets, we get  $\mathbf{r}$  samples by

$$\mathbf{r} = \begin{bmatrix} -\tan \varepsilon \cdot \cos \psi \\ -\tan \varepsilon \cdot \sin \psi \end{bmatrix}, \forall \varepsilon \in \mathcal{E}, \forall \psi \in \Psi,$$

subject to,

$$\bar{\varrho}_w \leq |\arctan_2(\mathbf{r}_{y,ICM,w}, \mathbf{r}_{x,ICM,w})| - \frac{\pi}{2} \leq \bar{\delta}_w$$

$$\mathbf{r}_{ICM,w}, \bar{\delta}_w \in \mathcal{D}_{ulim}, \bar{\varrho}_w \in \mathcal{D}_{llim}, \forall \mathbf{w} \in \mathbf{W}.$$

The rotation speed  $\omega$  can be directly sampled in a certain range. However, as  $r$  increases, certain rotation speeds may cause the traveling distance to be too long, so we set the longest arc length to control the farthest traveling distance of each step. The sampled  $\omega$  can be confined by a maximum curvature length. The sampling results of different steering limits are demonstrated in fig. 4. Through simple mathematical derivation according to eq. 1, we can obtain the current speed  $\Delta v$  and next position  $\Delta x$  after a certain time under this  $r$  and omega. Also, we can derive the relative wheel speed  $v_{w,n}$  and steering angle  $\delta_w, n$  of that node according to eq. 2, and eq. 4. It is worth noting that for the common situation where the limit angle is less than 90 degrees, there is a single mapping relationship between the wheel angle speed and the wheel friction point speed. If it exceeds 90 degrees, an additional mapping table will be needed. We will not discuss this for the time being. We add the speed and position values as attributes of the next point to the new node constructed during the hybrid A\* search. In order to better utilize the speed attribute of the node, we express the cost in time to unify the cost function and avoid weight adjustment of speed and distance information. So the traveling cost is computed by,

$$t_{v_w} = \frac{\max(|v_{w,n} - v_{w,n-1}|)}{\dot{v}_{w,max}}$$

$$t_{\delta_w} = \frac{\max(|\delta_{w,n} - \delta_{w,n-1}|)}{\dot{\delta}_{w,max}}$$

$$t_w = \sqrt{k_{v_w} t_{v_w}^2 + k_{\delta_w} t_{\delta_w}^2}, k_{v_w}, k_{\delta_w} \in \mathbb{R},$$

$$t_{body} = \max\left(\frac{\Delta x}{v_{max}}, \frac{\Delta \theta}{\dot{\theta}_{max}}\right),$$

$$\Delta g := \max(t_w, t_{body}), \forall \mathbf{w} \in \mathbf{W}.$$

The heuristic term is proportional to the Euler distance to the goal, which is calculated by

$$\hat{t}_v = \frac{\sqrt{(x_{goal} - x)^2 + (y_{goal} - y)^2}}{v_{max}}$$

$$\hat{t}_\theta = \frac{(\theta_{goal} - \theta)}{\dot{\theta}_{max}},$$

$$h := k_h \cdot \max(\hat{t}_v, \hat{t}_\theta), k_h \in \mathbb{R},$$

where  $k_h$  is the hypothesis coefficient, which represents the ratio of the time consumption of locomotion to the time consumption of the vehicle's motion with the maneuver. The algorithm is the same as ordinary hybrid A\* in the unmentioned aspects. The discretization search process of initial guess will also output the wheel steering and vehicle discontinuous state space flags, which will be explained in the next section.

### C. Trajectory Optimization

We choose the fourth-order Runge-Kutta method to ensure continuity between states at different times within time horizon  $T$ , as shown by the formula:

$$\mathbf{x}(t + dt) = \mathbf{x}(t) + \frac{1}{6}(k_1 + 2k_2 + 2k_3 + k_4),$$

where,  $\mathbf{x}(t)$  represents the states at time  $t$ ,  $dt$  is a short time duration,  $k_1, k_2, k_3, k_4$  are estimated slopes by the ordinary differential equation  $\frac{d\mathbf{x}}{dt} = \dot{\mathbf{x}} = [\dot{x} \quad \dot{y} \quad \dot{\theta} \quad \mathbf{u}^T]^T$ , by this case, the continuous constrain between  $\mathbf{x}(t)$  and  $\mathbf{x}(t + dt)$  is

$$G_c := \mathbf{x}(t + dt) - RK4(\mathbf{x}(t), \mathbf{u}(t), dt), \forall t \in [0, T].$$

We simplify the calculation of wheel angle by calculating the wheel's speed vector and rotation angle limit vector. **Steering limit constraints** can be modeled by

$$G_{\delta_{lim}} := \mathbf{v}_{r,w} \times \begin{bmatrix} \cos(\bar{\delta}_{lim}) \\ \sin(\bar{\delta}_{lim}) \end{bmatrix} \cdot \mathbf{v}_{r,w} \times \begin{bmatrix} \cos(\underline{\delta}_{lim}) \\ \sin(\underline{\delta}_{lim}) \end{bmatrix} \leq 0, \\ \forall t \in [0, T], \forall w \in \mathbf{W}.$$

When the steering range is larger than 180, this term can be removed.

**Mode changing constraints:** The control continuous space is divided into phases. The wheel rotation directions are provided by the initial guess. The rotating directions  $D_w \in \{-1, 1\}$  are searched according to the mapping table, minimum cost directions are selected if the steering ranges are overlapped. The determination of the direction of this round of rotation can be modeled as a Mixed Integer Nonlinear Optimization (MINLP) [31] problem, but its solution time is very long. The hybrid A\* process reduced the online optimization burden that may be introduced by MINLP.

In order to avoid the discontinuity problem caused by the atan2 function near the boundary of its value range, we use the vector angle method to measure the steering size between the two frames before and after.

$$G_{\delta_{lim}} := D_{w,t} \mathbf{v}_{r,w,t} \cdot D_{w,t-1} \mathbf{v}_{r,w,t-1} \\ - |\mathbf{v}_{r,w,t}| \cdot |\mathbf{v}_{r,w,t-1}| * \cos(\delta_{lim} * dt) \geq 0.$$

In addition to this, due to the discontinuity in the speed state space when switching wheel modes. Hybrid A\* also provides an indicator for manipulation phase  $M \in \mathbb{N}^{H \times 1}$  transition keyframes. The first and last frames of different modes are set as keyframes, and the speed of this frame is 0, which can be expressed by the equation as

$$G_M := v_t * (|M(t) - M(t + dt)| + |M(t) - M(t - dt)|) = 0.$$

To optimize total time and release unfeasible time constraints in the initial guess,  $\mathbf{dt}$  set is also optimized.

$$G_t := \mathbf{dt}\{dt | dt \in \mathbb{R}^+, dt \in [dt, \bar{dt}]\}.$$

The objective function is to minimize the total time and the control input.

$$\min J = \int_0^T F(\mathbf{x}, t) dt + \int_0^T \mathbf{u}(t)^T \mathbf{A} \mathbf{u}(t) dt + T,$$

in discrete mode

$$\min J = \sum_{h=0}^H F(\mathbf{x}, h) + \sum_{h=0}^H \mathbf{u}(h)^T \mathbf{A} \mathbf{u}(h) dt(h) + \sum_{h=0}^H dt(h),$$

s.t.:

$$\mathbf{x}(0) = \hat{\mathbf{x}}_0, \mathbf{x}(H) = \hat{\mathbf{x}}_f,$$

$$G_c, G_{v_w}, G_{\delta_{lim}}, G_{\delta_{lim}}, G_M, G_t,$$

where  $\mathbf{A}$  is the diagonal coefficient matrix,  $T$  is the total time,  $\mathbf{u}(t)$  is the state vector,  $\bar{\mathbf{x}}_0$  and  $\bar{\mathbf{x}}_f$  are the initial and final states,  $H$  is the sampling steps in the time horizon, and  $k_t$  is the weight of time optimization,  $F$  is an arbitrary task-related cost function. Here we make the distance between original waypoints and smoothed trajectory as the task-oriented cost function. Besides, **wheel acceleration** can be constrained with eq. 5 itself, avoiding complex computation in eq. 6.

## IV. EXPERIMENTS

### A. Constrained Trajectory Optimization

In experiments, we employed the open-source software CasADi [32] to facilitate the automatic differentiation of equations. For numerical optimization, we utilized IPOPT [33], a widely adopted and efficient nonlinear programming solver, to solve the optimization problems posed by our research. The experiments were conducted on a hardware platform featuring an Intel i9 12900K processor.

To validate the effectiveness of the C-AWS trajectory generator, we present optimized trajectories with turning angle limitations set at  $\pm 90^\circ$  and  $\pm 75^\circ$  in Fig. 5. Our optimizer can effectively confine the solution within the prescribed turning angle constraints for the wheels, which can be seen from the previous frame approaching the turn. The  $\pm 90^\circ$  steering limit allows for a larger lateral angle than  $\pm 75^\circ$ . The vehicle also successfully changed from a forward movement mode to a backward movement mode, while avoiding the in-situ rotation mode that requires two stops. Moreover, the optimized trajectories exhibit improved smoothness compared with initial guesses, which can be observed from ICM moving smoother and closer to the vehicle, especially when the vehicle is turning.

We verified that our model is applicable to different forms of chassis layouts with good robustness. The experiments are conducted by restricting the steering angle range of the rear wheel to  $\pm 0.001^\circ$  while limiting the front wheel's angular range to  $\pm 75^\circ$  to mimic bicycle models with different wheelbase and control center. Experimental results demonstrate that regardless of how we position the wheels, the ICM converges to compliant positions within these constraints as shown in



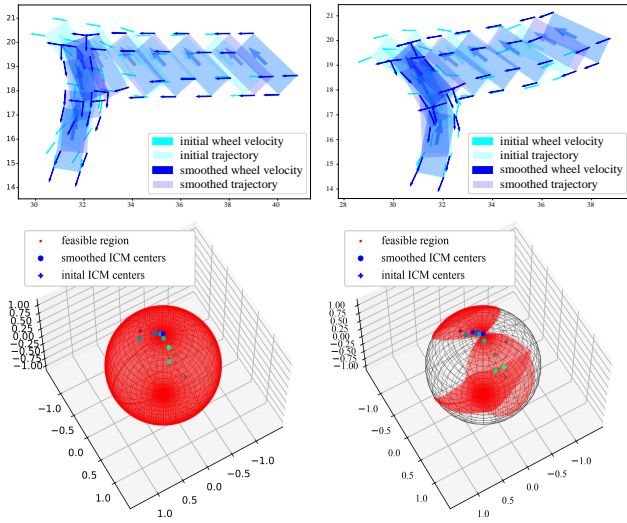


Fig. 5. For both Fig.5 and Fig.6, in upper figures, the initial and refined trajectory sequences are represented in cyan and blue, the arrow indicating the direction of wheel speeds. In lower figures, plus (+) indicate the ICM relative locations before optimization in the spherical coordinate system [6], while bullets (•) represent post-optimization positions, and the red zone indicates the feasible solution of ICMs. The color of the dot gradually transitions from blue to green as time progresses. In Fig.5, front and rear steering limits are set to  $\pm 90^\circ$  and  $\pm 75^\circ$  in the left and right columns respectively.

Fig. 6. In this experiment, the initial guesses were explored under conditions where both front and rear wheels are constrained to a  $\pm 75^\circ$  limit, and the model self-converges to states that adhere to the constraints in subsequent steps. This indicates that our model possesses good robustness, as it can tolerate some errors in the initial guess. In addition, we found that for forward sampling simulation processes, the choice of the control center should ensure that a sufficient number of effective sampling points are available. In the case of the bicycle model, setting the control center at the center of the rear axle generally offers a better path to approaching the goal.

### B. Trajectory Following Experiments

We conducted the trajectory following experiments in NVIDIA Isaac Sim [34] simulator, which can offer a realistic physics engine and accurate robot status. The simulator allows us to thoroughly develop and test our trajectory generator with high repeatability and flexibility. These evaluations were primarily carried out in a car park environment as Fig. 7 where precise and agile maneuvers are essential. To minimize the impact of the controller, the path followers are the same as C-AWS trajectory generators except the time horizon is much shorter. Velocity commands of the vehicle body are subsequently translated into specific velocity and angular commands for each wheel in the Vehicle Control Unit (VCU) at a rate of  $\sim 10Hz$ .

In Fig. 8, we sequentially compare the motion records of trajectory generators: OMNI-directional moving without steering limit constraint, front-rear symmetrical steering AWS (S-AWS), and our C-AWS generator. We have quantitatively assessed the degree of wheel slippage by slide ratio  $\lambda$ ,

$$\lambda = \max_{wheel} \left( v_{wheel} \cdot \cos \left( \delta_{real}^{wheel} - \delta_{ref}^{wheel} \right) \right),$$

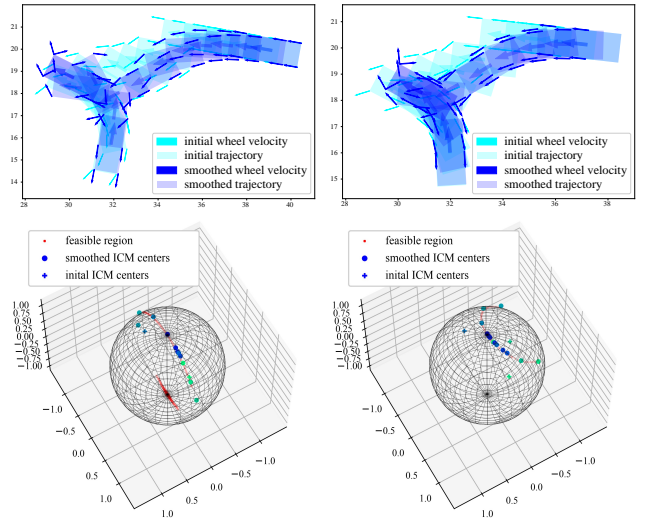


Fig. 6. The rear steering limits are set to  $\pm 0.001^\circ$  and the front steering limits are both  $\pm 75^\circ$ . The position of the rear wheel to the control center point is symmetrical with the front wheel in the left column. The position of the rear wheels is moved forward to both sides of the control center point, similar to the bicycle model in the right figure.

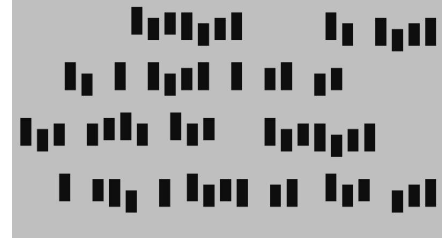


Fig. 7. The map of the experiment parking scene.

where the reference steering  $\delta_{ref}$  for each wheel comes from the ideal state the vehicle should be in under the recorded moving speed. The  $\lambda$  along time steps are shown in Fig. 9.

From the first row in Fig. 8, 9, it is evident that due to the absence of foreseeing steering constraints in OMNI, the wheels experience substantial unexpected jittering and slippage at discontinuous points in the control space, which in turn negatively impacts both the accuracy of trajectory tracking and the execution speed. In the second row in Fig. 8, 9, the optimal trajectory is generated using S-AWS, whose chassis geometry can also be considered as a standard bicycle model with a half-wheel base. From the figures, there are noticeable trade-offs as the vehicle's posture adjustments consume a significant amount of time, thereby prolonging the overall execution time. Indeed, due to the matching rotation angles of both the front and rear wheels of this chassis, it is inherently less susceptible to slipping. By contrast, our C-AWS optimizer facilitates the robot with more flexibility and completes the route with less time, and lower tracking error, while also exhibiting reduced wheel slippage, which can be readily drawn from the third row in Fig. 8, 9.

### C. Quantitative Comparison

We further verify the dynamic performance and computational efficiency of our algorithm. The experiments were

TABLE I  
DYNAMIC PERFORMANCE COMPARISON(UNITS: M, S, RAD)

Method	$\Delta d $	$\Delta\theta$	slide ratio $\lambda$	ave. velocity			ave. acceleration			ave. jerk		
				$v_x$	$v_y$	$v_{yaw}$	$a_x$	$a_y$	$a_{yaw}$	$j_x$	$j_y$	$j_{yaw}$
OMNI	0.236	0.167	0.069±0.24	1.161	0.838	0.186	0.398	0.352	0.156	29.77	26.14	11.96
S-AWS	0.214	0.140	0.015±0.08	1.463	0.068	0.187	0.305	0.157	0.145	1.261	1.200	0.640
w/o smooth	0.650	0.224	0.056±0.18	1.770	0.620	0.180	0.423	0.338	0.186	2.481	2.315	1.045
C-AWS(ous)	0.154	0.108	0.008±0.04	1.336	0.561	0.125	0.294	0.214	0.076	1.732	1.298	0.801

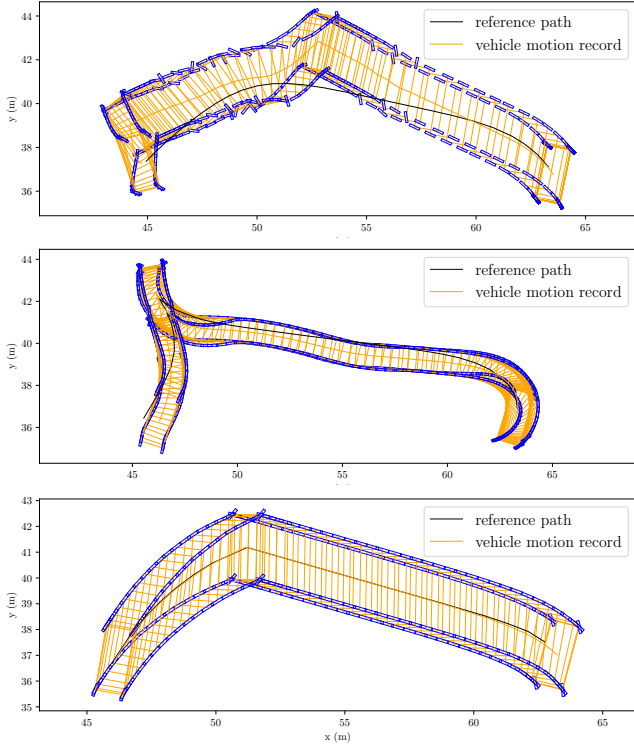


Fig. 8. Smoothed paths and motion records are depicted in the simulator. The robots are tasked with locomoting from the pose on the right to the left. The black line represents the reference path, while the orange line indicates the recorded control center. Additionally, the orange and blue rectangles illustrate the recorded body and wheel noses, respectively.

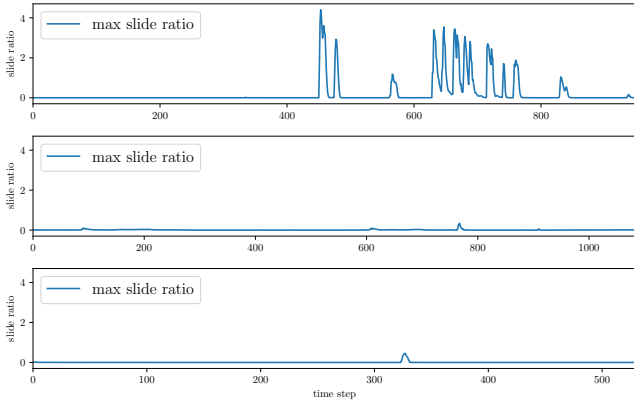


Fig. 9. The max slide ratio among wheels during trajectory following process.

conducted in the same setup as section IV-B. Each group of experiments randomly sampled 100 pairs of starting points and ending points in a parking lot environment and then allowed the vehicle to complete tracking of the trajectory under the instructions of the controller.

TABLE II  
OPERATION TIME COMPARISON(UNITS: S)

Method	Success Rate	Search 20steps	Optimize 20steps	Headless 20steps
OMNI	99.00%	2.9537 ±9.7958	0.2467 ±0.2083	0.1137 ±0.0571
S-AWS	100.00%	0.8038 ±0.7884	2.1572 ±0.4868	1.3876 ±0.3268
C-AWS(ours)	98.00%	0.5994 ±1.4477	1.5680 ±1.2595	0.9678 ±1.0592

We quantitatively evaluated the aforementioned trajectory generator and followers, including **OMNI**: to prove the impact on vehicle motion if the steering constraint is ignored; **S-AWS**: to prove the generalization of our proposed method and that it can satisfy the basic model of the bicycle model; **C-AWS**: to prove it really works and illustrate its properties. We additionally add baseline **w/o smooth** by directly feeding the trajectory generated through hybrid A\* to the trajectory tracking controller for tracking. The comparison with this baseline is mainly to prove the contribution of our proposed method to the smoothness of vehicle driving and the ease of trajectory tracking.

From Table I we can see that the method we proposed has a lower wheel slide ratio, which can lead to more stable control and less mechanical damage to the vehicle during driving. And there is smaller acceleration during driving, which can better ensure the comfort of the passengers and the safety of the cargo carried. By comparing with **w/o smooth**, the transformation speed before optimization is faster, but this is achieved by sacrificing the acceleration and deceleration process and traceability performance. The operation times are listed in Table II. Compared with **OMNI** who despite the wheel constraints, our method illustrates that computation of wheel constraints will lead to a longer trajectory planning time, they can still basically meet the real-time requirements of the trajectory planning module. Furthermore, we computed the optimization time excluding the initialization time. The data reveals that our running time still retains approximately 40% optimization potential.

## V. CONCLUSION AND DISCUSSION

In this work, we addressed the trajectory planning problem for constrained all-wheel steering (AWS) robots. We employed a search-first-then-optimize framework, reformulating the AWS kinematic model to tackle the nonlinearity arising from steering limits. In this framework, a time-cost-2nd-order initial trajectory planner was introduced. It was widely suitable for robots with fixed steering axis positions. Additionally, a

trajectory optimizer that incorporates our kinematic model was proposed, linearizing steering constraints to generate feasible paths and control mechanisms for C-AWS. Our approach not only enhanced maneuverability but also improved passenger comfort by reducing acceleration changes. Compared to alternatives, our method was superior and met the requirements for real-time operation.

For future work, we aim to enhance the efficiency of our method by optimizing the running speed of the search and optimization processes. We also plan to integrate our approach with various tasks to assess how this type of chassis can be improved for different applications. Additionally, the constrained AWS (C-AWS) system will be upgraded with modern differentiable collision-avoidance algorithms [29]. These improvements will be applicable in both static and dynamic environments, promising safer and more efficient transportation.

#### REFERENCES

- [1] G. Mouriaux, C. Novales, G. Poisson, and P. Vieyres, "Omni-directional robot with spherical orthogonal wheels: concepts and analyses," in *Proceedings 2006 IEEE International Conference on Robotics and Automation, 2006. ICRA 2006.*, 2006, pp. 3374–3379.
- [2] R. Cao, J. Gu, C. Yu, and A. Rosendo, "Omniwheg: An omnidirectional wheel-leg transformable robot," in *2022 IEEE/RSJ International Conference on Intelligent Robots and Systems (IROS)*, 2022, pp. 5626–5631.
- [3] T. L. Lam, H. Qian, and Y. Xu, "Omnidirectional steering interface and control for a four-wheel independent steering vehicle," *IEEE/ASME Transactions on Mechatronics*, vol. 15, no. 3, pp. 329–338, 2010.
- [4] T. M. Howard and A. Kelly, "Trajectory and spline generation for all-wheel steering mobile robots," in *2006 IEEE/RSJ International Conference on Intelligent Robots and Systems*, 2006, pp. 4827–4832.
- [5] J. Pentzer, S. Brennan, and K. Reichard, "Model-based prediction of skid-steer robot kinematics using online estimation of track instantaneous centers of rotation," *Journal of Field Robotics*, vol. 31, no. 3, pp. 455–476, 2014.
- [6] C. P. Connette, A. Pott, M. Hagele, and A. Verl, "Control of an pseudo-omnidirectional, non-holonomic, mobile robot based on an icm representation in spherical coordinates," in *2008 47th IEEE conference on decision and control*. IEEE, 2008, pp. 4976–4983.
- [7] R. Oftadeh, R. Ghabcheloo, and J. Mattila, "Time optimal path following with bounded velocities and accelerations for mobile robots with independently steerable wheels," in *2014 IEEE International Conference on Robotics and Automation (ICRA)*. IEEE, 2014, pp. 2925–2931.
- [8] —, "Universal path-following of wheeled mobile robots: A closed-form bounded velocity solution," *Sensors*, vol. 21, no. 22, p. 7642, 2021.
- [9] G. Champion, G. Bastin, and B. Dandrea-Novet, "Structural properties and classification of kinematic and dynamic models of wheeled mobile robots," *IEEE transactions on robotics and automation*, vol. 12, no. 1, pp. 47–62, 1996.
- [10] D. Dolgov, S. Thrun, M. Montemerlo, and J. Diebel, "Path planning for autonomous vehicles in unknown semi-structured environments," *The International Journal of Robotics Research*, vol. 29, no. 5, pp. 485–501, 2010. [Online]. Available: <https://doi.org/10.1177/0278364909359210>
- [11] R. M. Murray, M. Rathinam, and W. Sluis, "Differential flatness of mechanical control systems: A catalog of prototype systems," in *ASME international mechanical engineering congress and exposition*. Citeseer, 1995, pp. 349–357.
- [12] A. Gfrerrer, "Geometry and kinematics of the mecanum wheel," *Computer Aided Geometric Design*, vol. 25, no. 9, pp. 784–791, 2008.
- [13] M. S. Saidonr, H. Desa, and M. N. Rudzuan, "A differential steering control with proportional controller for an autonomous mobile robot," in *2011 IEEE 7th International Colloquium on Signal Processing and its Applications*. IEEE, 2011, pp. 90–94.
- [14] M. W. Choi, J. S. Park, B. S. Lee, and M. H. Lee, "The performance of independent wheels steering vehicle(4ws) applied ackerman geometry," in *2008 International Conference on Control, Automation and Systems*, 2008, pp. 197–202.
- [15] R. M. Murray and S. S. Sastry, "Nonholonomic motion planning: Steering using sinusoids," *IEEE transactions on Automatic Control*, vol. 38, no. 5, pp. 700–716, 1993.
- [16] C. Urmson, J. Anhalt, D. Bagnell, C. Baker, R. Bittner, M. Clark, J. Dolan, D. Duggins, T. Galatali, C. Geyer *et al.*, "Autonomous driving in urban environments: Boss and the urban challenge," *Journal of field Robotics*, vol. 25, no. 8, pp. 425–466, 2008.
- [17] M. McNaughton, C. Urmson, J. M. Dolan, and J.-W. Lee, "Motion planning for autonomous driving with a conformal spatiotemporal lattice," in *2011 IEEE International Conference on Robotics and Automation*. IEEE, 2011, pp. 4889–4895.
- [18] M. Ruffi and R. Siegwart, "On the design of deformable input- / state-lattice graphs," in *2010 IEEE International Conference on Robotics and Automation*, 2010, pp. 3071–3077.
- [19] S. LaValle, "Rapidly-exploring random trees: A new tool for path planning," *Research Report 9811*, 1998.
- [20] D. J. Webb and J. Van Den Berg, "Kinodynamic rrt\*: Asymptotically optimal motion planning for robots with linear dynamics," in *2013 IEEE international conference on robotics and automation*. IEEE, 2013, pp. 5054–5061.
- [21] L. Palmieri, S. Koenig, and K. O. Arras, "Rrt-based nonholonomic motion planning using any-angle path biasing," in *2016 IEEE International Conference on Robotics and Automation (ICRA)*, 2016, pp. 2775–2781.
- [22] Y. Lin and S. Saripalli, "Path planning using 3d dubins curve for unmanned aerial vehicles," in *2014 international conference on unmanned aircraft systems (ICUAS)*. IEEE, 2014, pp. 296–304.
- [23] D. Dolgov and S. Thrun, "Autonomous driving in semi-structured environments: Mapping and planning," in *2009 IEEE international conference on robotics and automation*. IEEE, 2009, pp. 3407–3414.
- [24] W. Zeng, W. Luo, S. Suo, A. Sadat, B. Yang, S. Casas, and R. Urtasun, "End-to-end interpretable neural motion planner," in *Proceedings of the IEEE/CVF Conference on Computer Vision and Pattern Recognition*, 2019, pp. 8660–8669.
- [25] K. Kondak and G. Hommel, "Computation of time optimal movements for autonomous parking of non-holonomic mobile platforms," in *Proceedings 2001 ICRA. IEEE International Conference on Robotics and Automation (Cat. No. 01CH37164)*, vol. 3. IEEE, 2001, pp. 2698–2703.
- [26] D. Lam, C. Manzie, and M. Good, "Model predictive contouring control," in *49th IEEE Conference on Decision and Control (CDC)*, 2010, pp. 6137–6142.
- [27] H. Shin, D. Kim, and S.-E. Yoon, "Kinodynamic comfort trajectory planning for car-like robots," in *2018 IEEE/RSJ International Conference on Intelligent Robots and Systems (IROS)*. IEEE, 2018, pp. 6532–6539.
- [28] W. Ding, L. Zhang, J. Chen, and S. Shen, "Safe trajectory generation for complex urban environments using spatio-temporal semantic corridor," *IEEE Robotics and Automation Letters*, vol. 4, no. 3, pp. 2997–3004, 2019.
- [29] Z. Han, Y. Wu, T. Li, L. Zhang, L. Pei, L. Xu, C. Li, C. Ma, C. Xu, S. Shen *et al.*, "An efficient spatial-temporal trajectory planner for autonomous vehicles in unstructured environments," *IEEE Transactions on Intelligent Transportation Systems*, 2023.
- [30] A. Dontchev and W. Hager, "The euler approximation in state constrained optimal control," *Mathematics of Computation*, vol. 70, no. 233, pp. 173–203, 2001.
- [31] J. Kronqvist, D. E. Bernal, A. Lundell, and I. E. Grossmann, "A review and comparison of solvers for convex minlp," *Optimization and Engineering*, vol. 20, pp. 397–455, 2019.
- [32] J. A. E. Andersson, J. Gillis, G. Horn, J. B. Rawlings, and M. Diehl, "CasADi – A software framework for nonlinear optimization and optimal control," *Mathematical Programming Computation*, vol. 11, no. 1, pp. 1–36, 2019.
- [33] A. Wächter and L. T. Biegler, "On the implementation of an interior-point filter line-search algorithm for large-scale nonlinear programming," *Mathematical programming*, vol. 106, pp. 25–57, 2006.
- [34] J. Liang, V. Makoviychuk, A. Handa, N. Chentanez, M. Macklin, and D. Fox, "Gpu-accelerated robotic simulation for distributed reinforcement learning," in *Conference on Robot Learning*. PMLR, 2018, pp. 270–282.